Numerical analysis of nonlinear wave propagation in a pantographic sheet

Simon R. Eugster[1]

[1]Institute for Nonlinear Mechanics
University of Stuttgart
Pfaffenwaldring 9, 70569 Stuttgart, Germany

Abstract: To study nonlinear wave propagation phenomena in pantographic sheets, we propose a dynamic model that consists of an assembly of interconnected planar nonlinear Euler–Bernoulli beams. The interconnections are either formulated as perfect bilateral constraints or by one-dimensional generalized force laws. Accordingly, the spatially discretized system is described by a differential algebraic system of equations, which is solved with an appropriate numerical solution strategy. We analyze various wave propagation phenomena by changing the kind of excitation.

Keywords: microstructured continua, pantographic structures, wave propagation, nonlinear beam finite elements

1 Introduction

In recent years, mechanical metamaterials with pantographic microstructure have caught many researcher's attention [36, 8, 9, 17, 18]. The design of this particular microstructure has an exciting background. It is neither a micro-structure that appears in nature nor does it come from a profane idea such as the optimization of the strength to weight ratio. It results from curiosity-driven research and the desire to break the chains of the mainstream of Cauchy continuum mechanics, which assumes that interactions between subbodies take place exclusively by surface interactions, [39]. Restricting oneself to hyperelastic material behavior, Cauchy continua allow only for strain energy densities that depend on the first gradient of the body's placement function. Guided by the mathematical theory of calculus of variations and the mechanical principle of stationary potential energy [15, 37], an apparently straight forward extension of the theory of continuous bodies is to allow the strain energy density to depend also on higher gradients; this can be the second gradient [20, 21, 38, 34] or even the Nth gradient [16] of the placement function. A material with a pantographic microstructure exhibits the properties which can be described on a macro level by a higher gradient continuum [1, 5, 4].

One of the best-studied design of a pantographic sheet was proposed in [14]. Besides a 3D-printed materialization, which is visualized in Fig. 1, a homogenization procedure leads to a second gradient continuum describing the planar and static behavior of the sheet. Hence, the typical pantographic sheet is a structure composed of two layers, each consisting of parallel fibers. These layers lie on top of each other and are oriented such that the fibers intersect, in the top view, with an angle of 90 degrees. At every intersection, the fibers of the upper and lower layers are connected by a pin. Depending on the range of application, many different models have been proposed describing the static and also dynamic behavior of this structure. Certainly, the entire structure can be regarded as a three-dimensional elastic continuum that can be described by Cauchy continuum mechanics. This computationally expensive description is used in [22] to find suitable parameters for the planar description. In [11] and [25], similar identifications are used to obtain the parameters of shell models that describe also the out-of-plane deformation. Recently, a more refined shell model has been proposed that includes even the relative displacement and rotation between the upper and lower layer of fibers [26, 28]. For a vibration analysis of shell formulations with straight and non-straight fibers, we refer to [27] and [23], respectively.

Very simplistic but highly effective and computationally cheap models are discrete formulations, also known as Hencky-type formulations. They describe the planar behavior by interconnected extensional and torsional springs [41, 42]. Often this kind of description is at the bottom of a homogenization procedure, [14, 5].

Somewhat between discrete and continuum are models which describe the individual fibers as nonlinear beams, see [2, 10, 33]. Using beam formulations restricted to the small strain regime, a preliminary study of wave propagation phenomena is given in [13, 12]. In the context of higher gradient continuum models, [30, 31], [24] and [7] study the dynamics of the pantographic sheet, a one-dimensional pantographic continuum as well as the pantographic beam [6], respectively. In [40], the dynamics of the pantographic beam is also investigated using a discrete Hencky-type model.

In this paper, we propose a model to analyze the planar transient dynamic behavior of the pantographic sheet. As an extension of the static consideration in [33], we formulate a dynamic model composed of interconnected planar nonlinear beams. The behavior of the spatially discretized system is eventually captured by a differential algebraic system of equations (DAE). In order to introduce notation and kinematics, in Sect. 2, we recapitulate the theory and finite element formulation of the planar nonlinear Euler–Bernoulli beam from [19]. A similar formulation can also be found in [32]. Working within the variational framework of the principle of virtual

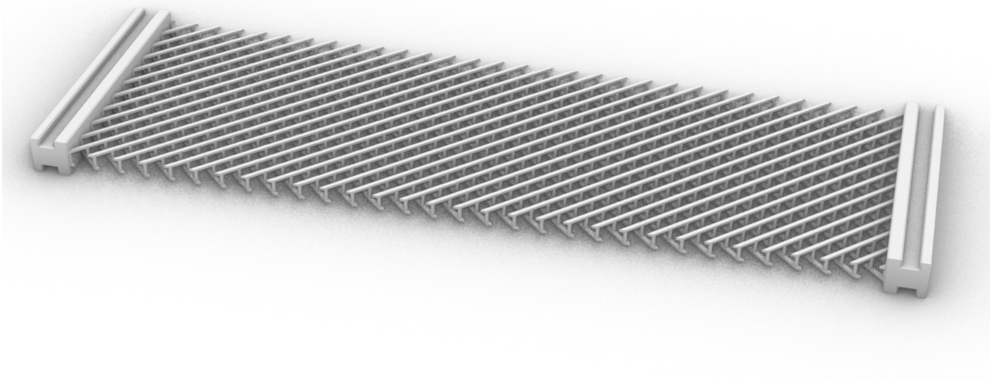

Figure 1: CAD visualization of the pantographic sheet, [28].

work, in Sect. 3, we model the pantographic sheet as a multibody system of interconnected discretized planar beams. The interactions as well as the boundary conditions are formulated either as perfect bilateral constraints or as generalized one-dimensional force laws. In Sect. 4, for various excitation functions, nonlinear wave propagation phenomena are investigated.

2 Nonlinear Euler–Bernoulli beam

The motion of the system is described in the two-dimensional Euclidean vector space $\mathbb{E}^2$ with origin O and orthonormal inertial frame given by the unit vectors $\mathbf{e}_x, \mathbf{e}_y \in \mathbb{E}^2$. If not otherwise indicated, all introduced vectorial quantities will be represented with respect to the inertial $\mathbf{e}_x$-$\mathbf{e}_y$-frame as tuples of real numbers. Often, there will also appear n-tuples of real numbers which will be treated in the sense of matrix multiplication as $\mathbb{R}^{n\times 1}$-matrices, i.e., as “column vectors”.

The motion of a planar nonlinear Euler–Bernoulli beam is represented by the centerline

$$\mathbf{x}(s,t) = (x(s,t), y(s,t)) \ , \tag{1}$$

which is a plane curve parametrized by the real-valued position functions $x = x(s,t)$ and $y = y(s,t)$, which in turn depend on time t and on $s \in [0, l]$ being the arc length of the undeformed beam with length l. Denoting with the prime $(\bullet)'$ the derivative with respect to the reference arc length s, the inclination angle $\theta = \theta(s,t)$ between the tangent vector $\mathbf{x}'$ and the horizontal

$\mathbf{e}_x$-direction can be computed as

$$\theta = \arctan\left(\frac{y'}{x'}\right) . \tag{2}$$

Consider $\hat{x} = \hat{x}(s,t,\varepsilon)$ and $\hat{y} = \hat{y}(s,t,\varepsilon)$ to be differentiable parametrizations with respect to $\varepsilon \in \mathbb{R}$ such that the actual positions are embedded in the parametrization and are obtained for $\varepsilon = 0$. Then, by replacing the corresponding functions in (1), the variational family $\hat{\mathbf{x}} = \hat{\mathbf{x}}(s,t,\varepsilon)$ is obtained. Introducing $\delta x = \partial\hat{x}/\partial\varepsilon|_{\varepsilon=0}$ and $\delta y = \partial\hat{y}/\partial\varepsilon|_{\varepsilon=0}$, the virtual displacement of the centerline $\delta\mathbf{x} = \delta\mathbf{x}(s,t)$ is defined as

$$\delta\mathbf{x} = \left.\frac{\partial\hat{\mathbf{x}}}{\partial\varepsilon}\right|_{\varepsilon=0} = (\delta x, \delta y) . \tag{3}$$

The extension of the beam is captured by the axial stretch $g = g(s,t)$, which, together with its variation $\delta g = \delta g(s,t)$, is defined as

$$g = \|\mathbf{x}'\| = [(x')^2 + (y')^2]^{1/2} , \quad \delta g = \frac{\delta\mathbf{x}'^\top\mathbf{x}'}{g} . \tag{4}$$

The curvature of the beam, which is the rate of change of the beams inclination angle, as well as the virtual rotation $\delta\theta = \delta\theta(s,t)$ induced by the variation of the centerline can be expressed as

$$\theta' = \frac{(\mathbf{x}'_\perp)^\top\mathbf{x}''}{g^2} , \quad \delta\theta = \frac{(\mathbf{x}'_\perp)^\top\delta\mathbf{x}'}{g^2} . \tag{5}$$

Note the introduced mapping $_\perp\colon \mathbf{a} = (a_1, a_2) \mapsto \mathbf{a}_\perp = (-a_2, a_1)$, which corresponds to a 90 degrees rotation in counterclockwise direction. Carrying out the variation of the curvature θ', together with the relation $(\delta\mathbf{x}'_\perp)^\top\mathbf{x}'' = -\delta\mathbf{x}'^\top\mathbf{x}''_\perp$, we get

$$\delta\theta' = \frac{1}{g^2}\Big((\mathbf{x}'_\perp)^\top\delta\mathbf{x}'' - \delta\mathbf{x}'^\top[2\theta'\mathbf{x}' + \mathbf{x}''_\perp]\Big) . \tag{6}$$

A hyperelastic planar nonlinear Euler–Bernoulli beam is characterized by a strain energy function per unit reference arc length $W = W(g,\theta')$. Henceforth, we choose the quadratic strain energy function for straight beams

$$W(g,\theta') = \frac{1}{2}k_\mathrm{e}(g-1)^2 + \frac{1}{2}k_\mathrm{b}\theta'^2 , \tag{7}$$

where k_e and k_b denote the beam's extensional and bending stiffnesses, respectively. The internal virtual work of a beam as the negative of the first variation of the beam's total strain energy is

$$\delta W_\mathrm{b}^\mathrm{int} = -\int_0^l \delta W \mathrm{d}s = -\int_0^l \left\{\frac{\partial W}{\partial g}\delta g + \frac{\partial W}{\partial\theta'}\delta\theta'\right\}\mathrm{d}s . \tag{8}$$

Identifying $N = \partial W/\partial g = k_\mathrm{e}(g-1)$ and $M = \partial W/\partial \theta' = k_\mathrm{b}\theta'$ as axial force and bending couple, respectively, and inserting (4) and (6) into (8), we get

$$\delta W_\mathrm{b}^\mathrm{int} = -\int_0^l \left\{ \frac{1}{g}\delta \mathbf{x}'^\top \left(\mathbf{x}'N - \frac{M}{g}[2\theta'\mathbf{x}' + \mathbf{x}''_\perp] \right) + \delta \mathbf{x}''^\top \mathbf{x}'_\perp \frac{M}{g^2} \right\} \mathrm{d}s \; . \tag{9}$$

The virtual work contribution of the inertial forces is given by

$$\delta W_\mathrm{b}^\mathrm{dyn} = -\int_0^l \delta \mathbf{x}^\top A_{\rho_0} \ddot{\mathbf{x}} \mathrm{d}s \; , \tag{10}$$

where A_{ρ_0} is the mass density per unit reference arc length and the dot $(\dot{\bullet})$ denotes the time derivative. Note, that we omitted the contribution that takes the rotatory inertia of the beam into account, compare [19, Sect. 7.2].

For a Galerkin-type finite element discretization of the beam, we approximate the centerline by B-spline polynomials. This approximation can be written in the form $\mathbf{x}(s,t) \approx \mathbf{r}(s, \mathbf{q}(t)) = \mathbf{N}(s)\mathbf{q}(t)$, where $\mathbf{N} = \mathbf{N}(s) \in \mathbb{R}^{2\times 2n_\mathrm{cp}}$ is the matrix of B-spline basis functions and $\mathbf{q} = \mathbf{q}(t) \in \mathbb{R}^{2n_\mathrm{cp}}$ is the vector consisting of the coordinates of the n_cp control points, see [35]. Using the same approximation for all induced quantities, e.g., $\delta \mathbf{x} \approx \delta \mathbf{r}' = \mathbf{N}'\delta\mathbf{q}$, the internal virtual work (9) is approximated as

$$\begin{aligned} \delta W_\mathrm{b}^\mathrm{int,h} &= \delta \mathbf{q}(t)^\top \mathbf{f}_\mathrm{b}^\mathrm{int}(\mathbf{q}) \; , \\ \mathbf{f}_\mathrm{b}^\mathrm{int} &= -\int_0^l \left\{ \frac{1}{g}\mathbf{N}'^\top \left(\mathbf{r}'N - \frac{M}{g}[2\theta'\mathbf{r}' + \mathbf{r}''_\perp] \right) + \mathbf{N}''^\top \mathbf{r}'_\perp \frac{M}{g^2} \right\} \mathrm{d}s \; , \end{aligned} \tag{11}$$

where $\delta \mathbf{q} = \partial \hat{\mathbf{q}}/\partial \varepsilon|_{\varepsilon=0}$ are the virtual displacements of the discretized finite dimensional system determined by the variational families $\hat{\mathbf{q}} = \hat{\mathbf{q}}(t,\varepsilon) \in \mathbb{R}^{2n_\mathrm{cp}}$. The discretization of the inertial virtual work leads to

$$\delta W_\mathrm{b}^\mathrm{dyn,h} = -\delta \mathbf{q}(t)^\top \mathbf{M}_\mathrm{b} \ddot{\mathbf{q}}(t) \; , \quad \mathbf{M}_\mathrm{b} = \int_0^l A_{\rho_0} \mathbf{N}^\top \mathbf{N} \mathrm{d}s \; , \tag{12}$$

where $\mathbf{M}_\mathrm{b}$ is the constant, symmetric and positive definite mass matrix of the discretized beam. We refer the reader to [29], for an introduction to the finite element approximation of planar beams and in particular for more technical details concerning the used shape functions as well as the elementwise implementation.

3 Pantographic sheet

As sketched in Fig. 2, the pantographic sheet with length L and height H is composed of n_row rows and n_col columns of straight beams each of which

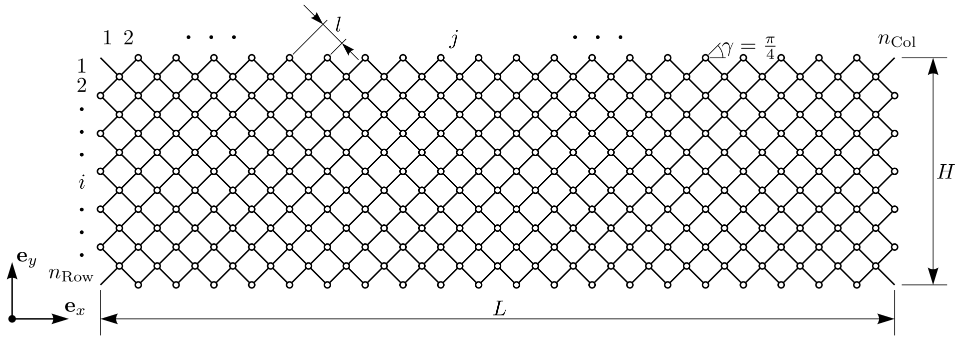

Figure 2: Reference configuration of the pantographic sheet.

has a reference length of $l = \sqrt{2}H/n_{\mathrm{row}}$. For convenience, both the number of rows and the number of columns are chosen to be even. In total there are $n_{\mathrm{b}} = n_{\mathrm{row}}n_{\mathrm{col}}$ individual beams, which are either addressed by the tuple (i, j) referring to row $i \in \{1, \dots, n_{\mathrm{row}}\}$ and column $j \in \{1, \dots, n_{\mathrm{col}}\}$ or by the index $b = (i-1)n_{\mathrm{col}} + j \in \{1, \dots, n_{\mathrm{b}}\}$. All beams are modeled as Euler–Bernoulli beams each with the same discretization that has been introduced in the previous section. Accordingly, the centerline $\mathbf{x}_b$ of beam b is approximated by $\mathbf{r}(s, \mathbf{q}_b(t)) = \mathbf{N}(s)\mathbf{q}_b(t)$. The generalized coordinates of the entire pantographic sheet, which are the control point coordinates of all beams, are collected in the tuple $\mathbf{q} = (\mathbf{q}_1, \dots, \mathbf{q}_{n_{\mathrm{b}}})$. The Boolean matrix $\mathbf{C}_b$ connects the beam coordinates $\mathbf{q}_b$ with the sheet coordinates $\mathbf{q}$ by means of $\mathbf{q}_b = \mathbf{C}_b\mathbf{q}$. In the reference configuration, as depicted in Fig. 2, the beams are arranged such that the $\mathbf{e}_x$-component of $\mathbf{r}(s, \mathbf{Q}_b)$ increases for increasing reference arc length s. Note that $\mathbf{Q}_b$ denotes the control point coordinates of beam b in the reference placement.

So far only n_{b} individual discretized beams have been introduced. To obtain a pantographic sheet, we propose a model with the following interactions:

1) *junction*: At the connection point of two adjacent beams within a single fiber, the beams must agree on their position and inclination angle.

2) *pivot*: At the intersection of the two fiber families, the corresponding beams show the same position throughout the motion.

3) *torsional spring:* In order to model the torsional stiffness of the pin that connects the two beam families, at each intersection, a torsional spring is added.

(i) longitudinal excitation 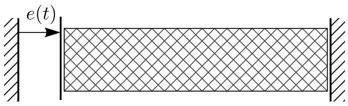	$i \in \{1, 3, \ldots, n_{\mathrm{row}}-1\} \cup \{n_{\mathrm{row}}\}$: $0 = \mathbf{e}_x^\top \mathbf{r}(0, \mathbf{q}_{i,1}) - e(t)$ $0 = \mathbf{e}_x^\top \mathbf{r}(l, \mathbf{q}_{i,n_{\mathrm{col}}}) - L$
(ii) lateral excitation 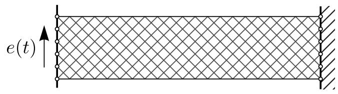	$i \in \{1, 3, \ldots, n_{\mathrm{row}}-1\} \cup \{n_{\mathrm{row}}\}$: $0 = \mathbf{r}(0, \mathbf{q}_{i,1}) - \mathbf{r}(0, \mathbf{Q}_{i,1}) - e(t)\mathbf{e}_y$ $0 = \mathbf{r}(l, \mathbf{q}_{i,n_{\mathrm{col}}}) - \mathbf{r}(l, \mathbf{Q}_{i,n_{\mathrm{col}}})$
(iii) point excitation 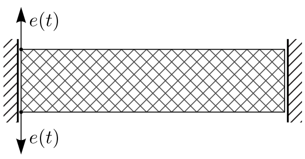	$i \in \{1, n_{\mathrm{row}}\}$: $0 = \mathbf{r}(0, \mathbf{q}_{i,1}) - \mathbf{r}(0, \mathbf{Q}_{i,1}) + (-1)^i e(t)\mathbf{e}_y$ $i \in \{3, \ldots, n_{\mathrm{row}}-1\}$: $0 = \mathbf{e}_x^\top \mathbf{r}(0, \mathbf{q}_{i,1})$ $i \in \{1, 3, \ldots, n_{\mathrm{row}}-1\} \cup \{n_{\mathrm{row}}\}$: $0 = \mathbf{e}_x^\top \mathbf{r}(l, \mathbf{q}_{i,n_{\mathrm{col}}}) - L$

Table 1: Boundary conditions in the form $\mathbf{g}^{\mathrm{bc}}(\mathbf{q}, t) = 0$.

4) *boundary conditions:* We consider here three different boundary conditions, which are listed in Tab. 1. For all boundary conditions the top and bottom edges are unconstrained. Moreover, there are no constraints that block the inclination angles of the beams.

   (i) *longitudinal excitation*: the boundary points of the left edge are excited in $\mathbf{e}_x$-direction with $e(t)$ and can move freely in $\mathbf{e}_y$-direction. The boundary points of the right edge are blocked in $\mathbf{e}_x$-direction but can move freely in $\mathbf{e}_y$-direction.

   (ii) *lateral excitation*: The boundary points of the left edge are excited in $\mathbf{e}_y$-direction with $e(t)$ and are blocked in $\mathbf{e}_x$-direction. At the right edge all beams are fixed.

   (iii) *point excitation*: While the top and bottom left corner points are excited by $e(t)$ in $\mathbf{e}_y$-direction, the left and right edge points are blocked in $\mathbf{e}_x$-direction but can move freely in $\mathbf{e}_y$-direction.

The interactions 1) through 3) with the corresponding virtual work contributions are exemplary introduced at an intersection point in the interior

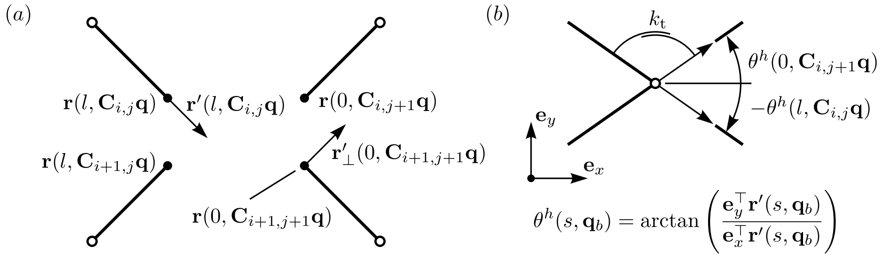

Figure 3: (a) Bilateral constraints at an interior intersection point. (b) Torsional pin stiffness with torsional spring.

of the sheet as depicted in Fig. 3.

junction: The junction within the bottom fiber family, $\gamma = -\pi/4$, is the perfect bilateral constraint with the constraint conditions

$$\mathbf{g}^{\text{jun}}(\mathbf{q}) = \begin{pmatrix} \mathbf{r}(l,\mathbf{C}_{i,j}\mathbf{q}) - \mathbf{r}(0,\mathbf{C}_{i+1,j+1}\mathbf{q}) \\ \mathbf{r}'(l,\mathbf{C}_{i,j}\mathbf{q})^\top \mathbf{r}'_\perp(0,\mathbf{C}_{i+1,j+1}\mathbf{q}) \end{pmatrix} = 0 \; . \tag{13}$$

Note the constraint condition on the inclination angle, which is formulated in terms of the tangent vectors. In fact, the angles of the adjacent beams agree if the tangent vector $\mathbf{r}'$ of beam (i,j) is perpendicular to the normal vector $\mathbf{r}'_\perp$ of beam $(i+1,j+1)$. The junction in the top beam family is obtained when exchanging the indices in (13) as follows: $(i,j) \mapsto (i+1,j)$ and $(i+1,j+1) \mapsto (i,j+1)$. Assuming the constraint to be perfect, the constraint conditions (13) are guaranteed by the virtual work contribution

$$\delta W^{\text{jun}} = \delta\mathbf{q}^\top \mathbf{W}^{\text{jun}}(\mathbf{q})\boldsymbol{\lambda}^{\text{jun}} \; , \quad \mathbf{W}^{\text{jun}} = \left(\frac{\partial \mathbf{g}^{\text{jun}}}{\partial \mathbf{q}}\right)^\top \; , \tag{14}$$

where $\mathbf{W}^{\text{jun}}$ and $\boldsymbol{\lambda}^{\text{jun}}$ denote the generalized force directions of the constraint and the Lagrange multipliers, respectively.

pivot: The constraint conditions of the pivot between the two fiber families are

$$\mathbf{g}^{\text{piv}}(\mathbf{q}) = \mathbf{r}(l,\mathbf{C}_{i,j}\mathbf{q}) - \mathbf{r}(0,\mathbf{C}_{i,j+1}\mathbf{q}) = 0 \; , \tag{15}$$

which demand the positions at the intersection to be the same. The virtual work contribution is given as

$$\delta W^{\text{piv}} = \delta\mathbf{q}^\top \mathbf{W}^{\text{piv}}(\mathbf{q})\boldsymbol{\lambda}^{\text{piv}} \; , \quad \mathbf{W}^{\text{piv}} = \left(\frac{\partial \mathbf{g}^{\text{piv}}}{\partial \mathbf{q}}\right)^\top \; . \tag{16}$$

torsional spring: Using the inclination angle of (2), the deviation from

$-\pi/2$ between the two fiber families is determined by

$$\mathrm{g}^{\mathrm{tor}}(\mathbf{q}) = \arctan\left(\frac{\mathbf{e}_y^\top \mathbf{r}'(l, \mathbf{C}_{i,j}\mathbf{q})}{\mathbf{e}_x^\top \mathbf{r}'(l, \mathbf{C}_{i,j}\mathbf{q})}\right) - \arctan\left(\frac{\mathbf{e}_y^\top \mathbf{r}'(0, \mathbf{C}_{i,j+1}\mathbf{q})}{\mathbf{e}_x^\top \mathbf{r}'(0, \mathbf{C}_{i,j+1}\mathbf{q})}\right) + \frac{\pi}{2} \ . \tag{17}$$

Using the quadratic potential $v(\mathrm{g}^{\mathrm{tor}}) = \frac{1}{2}k_{\mathrm{t}}(\mathrm{g}^{\mathrm{tor}})^2$, the virtual work for an individual torsional spring is

$$\delta W^{\mathrm{tor}} = -\delta v^{\mathrm{tor}}(\mathrm{g}^{\mathrm{tor}}(\mathbf{q})) = \delta\mathbf{q}^\top \mathbf{w}^{\mathrm{tor}}(\mathbf{q})\lambda^{\mathrm{tor}}(\mathbf{q}) \tag{18}$$

with the generalized force direction $\mathbf{w}^{\mathrm{tor}}$ and the force law given by

$$\mathbf{w}^{\mathrm{tor}} = \left(\frac{\partial \mathrm{g}^{\mathrm{tor}}}{\partial \mathbf{q}}\right)^\top \ , \quad \lambda^{\mathrm{tor}}(\mathbf{q}) = -k_{\mathrm{t}}\mathrm{g}^{\mathrm{tor}}(\mathbf{q}) \ . \tag{19}$$

boundary conditions: The boundary conditions are formulated as additional time dependent constraints with constraint equations $\mathbf{g}^{\mathrm{bc}}(\mathbf{q}, t) = 0$, which come along with the corresponding virtual work contribution

$$\delta W^{\mathrm{bc}} = \delta\mathbf{q}^\top \mathbf{W}^{\mathrm{bc}}(\mathbf{q}, t)\boldsymbol{\lambda}^{\mathrm{bc}} \ , \quad \mathbf{W}^{\mathrm{bc}} = \left(\frac{\partial \mathbf{g}^{\mathrm{bc}}}{\partial \mathbf{q}}\right)^\top \ . \tag{20}$$

The individual constraint equations that appear in $\mathbf{g}^{\mathrm{bc}}$ are specified in Tab. 1.

Summing up all these contributions, the total virtual work of the pantographic sheet with n_{b} beams can be written in the form

$$\delta W^{\mathrm{tot}} = -\delta\mathbf{q}^\top \left(\mathbf{M}\ddot{\mathbf{q}} - \mathbf{h}(\mathbf{q}) - \mathbf{W}(\mathbf{q}, t)\boldsymbol{\lambda}\right) \ , \tag{21}$$

with the constant, symmetric and positive definite mass matrix

$$\mathbf{M} = \sum_{b=1}^{n_{\mathrm{b}}} \mathbf{C}_b^\top \mathbf{M}_{\mathrm{b}} \mathbf{C}_b \ , \tag{22}$$

the generalized forces of all n_{b} beams and the n_{t} torsional springs

$$\mathbf{h}(\mathbf{q}) = \sum_{b=1}^{n_{\mathrm{b}}} \mathbf{C}_b^\top \mathbf{f}_{\mathrm{b}}^{\mathrm{int}}(\mathbf{C}_b\mathbf{q}) + \sum_{k=1}^{n_{\mathrm{t}}} \mathbf{w}_k^{\mathrm{tor}}(\mathbf{q})\lambda_k^{\mathrm{tor}}(\mathbf{q}) \ , \tag{23}$$

as well as the generalized force directions

$$\mathbf{W}(\mathbf{q}, t) = \Big(\mathbf{W}_1^{\mathrm{jun}}(\mathbf{q}) \cdots \mathbf{W}_{n_{\mathrm{j}}}^{\mathrm{jun}}(\mathbf{q}) \ \mathbf{W}_1^{\mathrm{piv}}(\mathbf{q}) \cdots \mathbf{W}_{n_{\mathrm{p}}}^{\mathrm{piv}}(\mathbf{q}) \ \mathbf{W}^{\mathrm{bc}}(\mathbf{q}, t)\Big) \ , \tag{24}$$

and Lagrange multipliers

$$\boldsymbol{\lambda} = (\boldsymbol{\lambda}_1^{\mathrm{jun}}, \dots, \boldsymbol{\lambda}_{n_{\mathrm{j}}}^{\mathrm{jun}}, \boldsymbol{\lambda}_1^{\mathrm{piv}}, \dots, \boldsymbol{\lambda}_{n_{\mathrm{p}}}^{\mathrm{piv}}, \boldsymbol{\lambda}^{\mathrm{bc}}) \tag{25}$$

geometric properties		kinetic properties	
n_{row}	12	k_{e}	500 N
n_{col}	300	k_{b}	417×10^{-7} Nm^2
H	$n_{\mathrm{row}} \times 0.01$ m	k_{t}	175×10^{-4} Nm
L	$n_{\mathrm{col}} \times 0.01$ m	A_{ρ_0}	93×10^{-5} kgm^{-1}
spatial discretization		**time discretization**	
# el./beam	1	t_{e}	8×10^{-2} s
polynomial degree	3	Δt	2×10^{-5} s
# quadr. points/el.	5	ρ_∞	0.8

Table 2: Model and discretization parameters.

arising from the n_{j} junctions, n_{p} pivots as well as the boundary conditions. The equations of motion of the pantographic sheet are obtained from the principle of virtual work, which holds along with the constraint conditions

$$\mathbf{g}(\mathbf{q}, t) = (\mathbf{g}_1^{\mathrm{jun}}(\mathbf{q}), \dots, \mathbf{g}_{n_{\mathrm{j}}}^{\mathrm{jun}}(\mathbf{q}), \mathbf{g}_1^{\mathrm{piv}}(\mathbf{q}), \dots, \mathbf{g}_{n_{\mathrm{p}}}^{\mathrm{piv}}(\mathbf{q}), \mathbf{g}^{\mathrm{bc}}(\mathbf{q}, t)) = 0 \ , \tag{26}$$

as the following differential algebraic system of equations

$$\begin{aligned} \mathbf{M}\ddot{\mathbf{q}} - \mathbf{h}(\mathbf{q}) - \mathbf{W}(\mathbf{q}, t)\boldsymbol{\lambda} &= 0 \ , \\ \mathbf{g}(\mathbf{q}, t) &= 0 \ . \end{aligned} \tag{27}$$

For the time integration of this semi-discrete equations of motion, we used the generalized-α scheme for constrained mechanical systems of index 3 proposed by [3].

4 Numerical Analysis and Discussion

As excitation function, see Fig. 4, we chose

$$e(t) = e_0 \sin\left(\frac{n\pi}{2s_1} t\right) \left(S_{1,[0,s_1]}(t) - S_{1,[s_1,2s_1]}(t)\right) \ , \tag{28}$$

where we made use of the first smooth step function S_{1,I_1} for the interval $I_1 = [a, b]$, which is defined as

$$S_{1,[a,b]}(t) = \begin{cases} 0 & t < a \ , \\ -2\left(\frac{t-a}{b-a}\right)^3 + 3\left(\frac{t-a}{b-a}\right)^2 & a \le t \le b \ , \\ 1 & b < t \ . \end{cases} \tag{29}$$

The excitation function (28) has the convenient property that the excitation velocity $\dot{e}$ is zero at $t = 0$ and $t = 2s_1$.

The analysis of the nonlinear wave propagation phenomena requires to solve the initial value problem given by the equations of motion (27) together with the initial values $\mathbf{q}(0) = \mathbf{Q}$, $\dot{\mathbf{q}}(0) = 0$ and $\boldsymbol{\lambda}(0) = 0$, where $\mathbf{Q}$ denotes the nodal coordinates of all individual beams in the reference configuration as sketched in Fig. 2. For each boundary condition, we computed the results for $s_1 = 0.01\,\mathrm{s}$ and $n = \{1, 2, 4\}$ and used model and discretization parameters listed in Tab. 2. The displacement e_0 was chosen for (i) the longitudinal excitation as $e_0 = 0.05\,\mathrm{m}$, for (ii) the lateral excitation as $e_0 = 0.05\,\mathrm{m}$, and for (iii) the point excitation as $e_0 = 0.03\,\mathrm{m}$.

In Figs. 5–7, time snapshots of the current configurations of the longitudinal excitation are shown. In order to visualize the contraction and dilatation of the sheet in $\mathbf{e}_y$-direction, the color map is associated with the positive and negative $\mathbf{e}_y$-displacement $u_y^{\pm} = \pm\mathbf{e}_y^{\top}(\mathbf{r}(s, \mathbf{q}(t)) - \mathbf{r}(s, \mathbf{Q}))$. The positive and negative $\mathbf{e}_y$-displacement u_y^+ and u_y^- is chosen for the beams above and below the horizontal symmetry line, respectively. In Fig. 5, one can see for $t \in [0, 0.02\,\mathrm{s}]$ how the positive longitudinal displacement causes a dilatation followed by a contraction of the sheet. While the dilatating wave packet decays very fast, the contracting wave packet travels through the sheet. Behind the contracting wave packet alternately dilatational and contracting wave packets emerge all of which travel at different speed. In Fig. 6, a similar behavior occurs in which the dilatational wave is not excited as much as for the first excitation. The excitation leads to contracting and dilatational wave packets that are much longer in $\mathbf{e}_x$-direction. For $n = 4$, in Fig. 7, the excitation causes dilatational and contracting wave packets that are much more localized.

For the lateral excitation, the snapshots in Figs. 8–10 are colored by the displacement in $\mathbf{e}_y$-direction, that is $u_y = \mathbf{e}_y^{\top}(\mathbf{r}(s, \mathbf{q}(t)) - \mathbf{r}(s, \mathbf{Q}))$. Both in Fig. 8 and Fig. 9 propagating lateral waves can be recognized. The shorter wave packets travel with a higher speed such that the wave propagation is highly dispersive. In Fig. 10, the nonlinearity of the problem causes an interaction between lateral and dilatational wave. Starting from $t = 0.03\,\mathrm{s}$, superposed to the lateral displacement, contracting and dilatating wave packets do appear.

For the point excitation in Figs. 11–13, the colormap is associated with the positive and negative $\mathbf{e}_y$-displacements as it is done for the longitudinal excitation. The wave propagation phenomena resemble the ones observed for the longitudinal excitation. In contrast to the longitudinal excitation, the excitation does not induce a dilatating wave packet that runs ahead of the first contracting wave packet. It can be recognized as a particular property of the pantographic sheet, that the longitudinal excitation as well as the pointwise excitation in lateral direction cause similar wave propagation

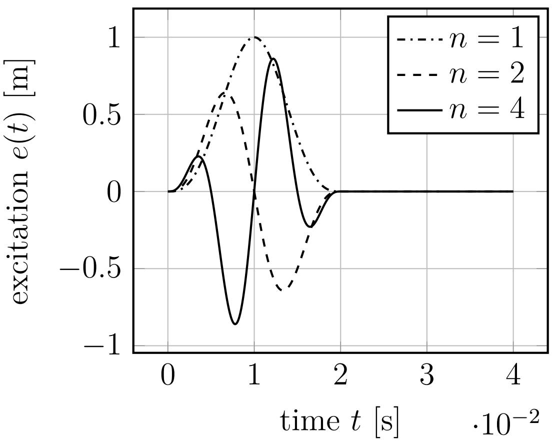

Figure 4: Excitation function for $s_1 = 1 \times 10^{-2}$ s.

phenomena.

In particular for the longitudinal and point excitations, the traveling wave packages at different speed are striking. With the current excitation functions these wave packages decay passing through the pantographic structure. However, since the change of the wave forms are not so drastic, we dare to conjecture that there may exist a certain excitation function for which a certain wave package travels through the structure without changing its form, i.e., that a solitary wave exists.

5 Conclusion

The main goal of the paper was to introduce a planar model to analyze nonlinear wave propagation phenomena in pantographic sheets. The proposed model can be seen as a multibody system consisting of planar Euler–Bernoulli beams that are coupled by perfect bilateral constraints and generalized one-dimensional force laws. The equations of motion are eventually characterized as a DAE of index 3 which is solved using a robust generalized-α scheme. The formulation within the variational framework of the principle of virtual work allows for a systematic extension of the presented model. Instead of a quadratic strain energy function for the beam, also other strain energy functions can be used. Moreover, dissipative mechanisms within the beams could be modeled by postulating the internal virtual work contribution of the beams together with constitutive laws for axial force and bending couple depending on the axial stretch, the curvature and time derivatives thereof. Also the interaction between the beam families can be extended easily by

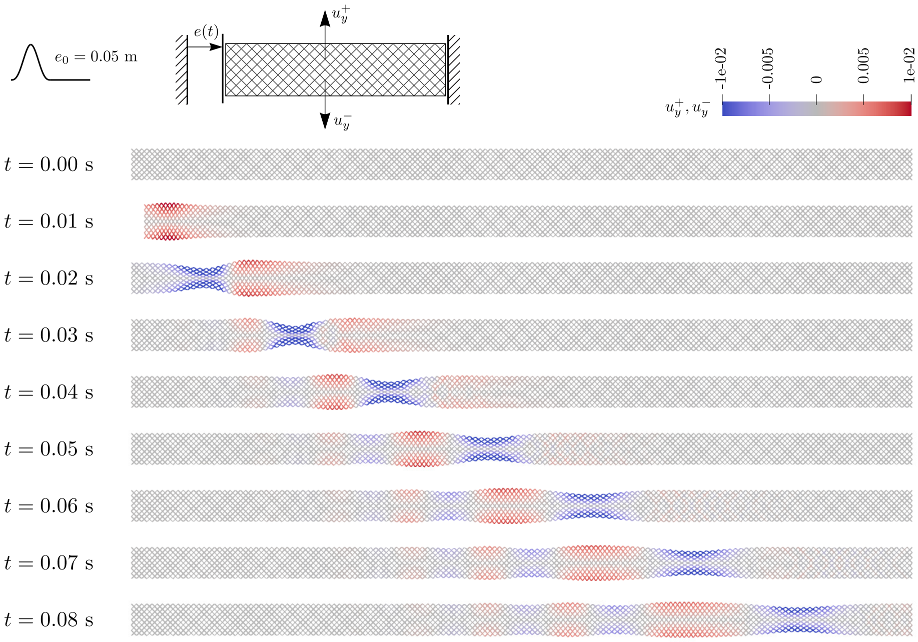

Figure 5: Longitudinal excitation with $n = 1, s_1 = 0.01\,\mathrm{s}$ and $e_0 = 0.05\,\mathrm{m}$.

changing the force law for the torsional spring.

The presented wave propagation phenomena were all highly dispersive. It is task for future investigations, to find out whether the conjecture of the existence of solitary waves is true or not. Solitary waves appear in structures where the nonlinearities compensate the dispersive effects in the wave propagation. If for the current formulation there does not exist a soliton, one might still find such a wave when considering the same structure with nonlinear constitutive laws for the beams and the torsional springs. One can think of two possibilities to approach this difficult problem. The first way is to develop a brute force numerical procedure testing a huge amount of excitation functions together with a method filtering out relevant wave packages. The second way is to work with the two-dimensional continuum limit which may allow for a further reduction to a one-dimensional continuum formulation. For such a reduced formulation either the envisaged brute force method or some analytical procedures can be applied.

References

[1] J.-J. Alibert, P. Seppecher, and F. dell'Isola. Truss modular beams with deformation energy depending on higher displacment gradient. *Mathe-*

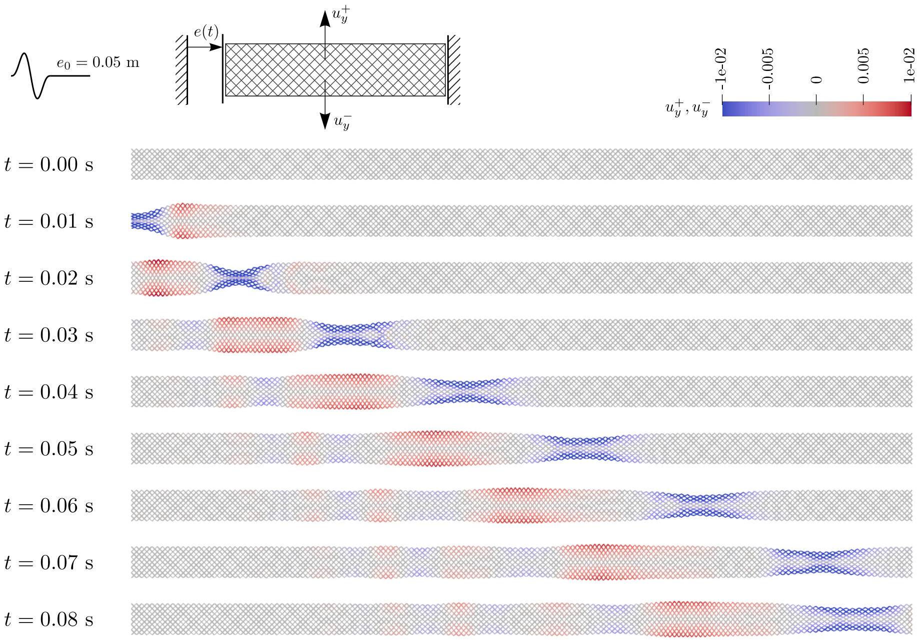

Figure 6: Longitudinal excitation with $n = 2, s_1 = 0.01\,\mathrm{s}$ and $e_0 = 0.05\,\mathrm{m}$.

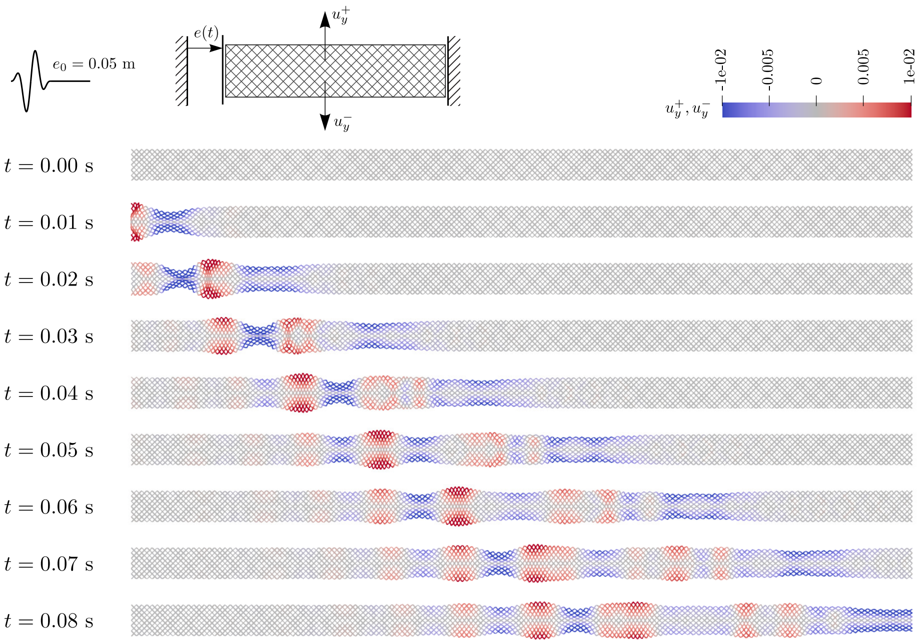

Figure 7: Longitudinal excitation with $n = 4, s_1 = 0.01\,\mathrm{s}$ and $e_0 = 0.05\,\mathrm{m}$.

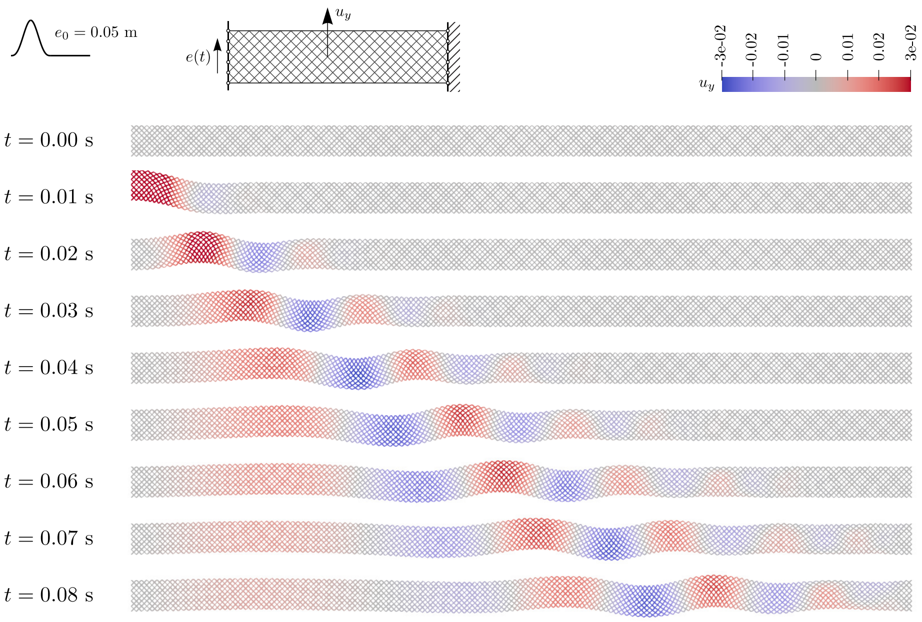

Figure 8: Lateral excitation with $n = 1, s_1 = 0.01\,\mathrm{s}$ and $e_0 = 0.05\,\mathrm{m}$.

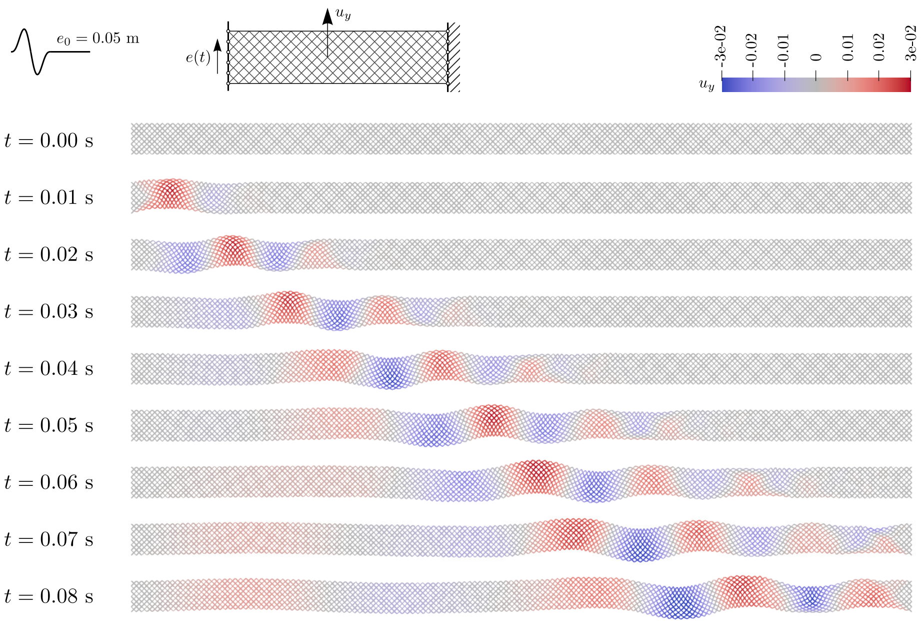

Figure 9: Lateral excitation with $n = 2, s_1 = 0.01\,\mathrm{s}$ and $e_0 = 0.05\,\mathrm{m}$.

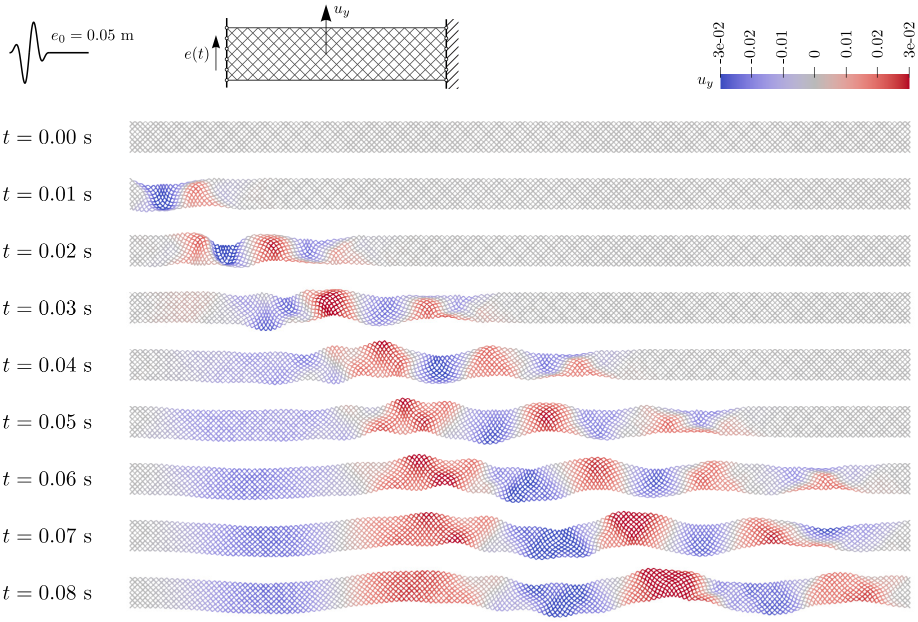

Figure 10: Lateral excitation with $n = 4, s_1 = 0.01\,\mathrm{s}$ and $e_0 = 0.05\,\mathrm{m}$.

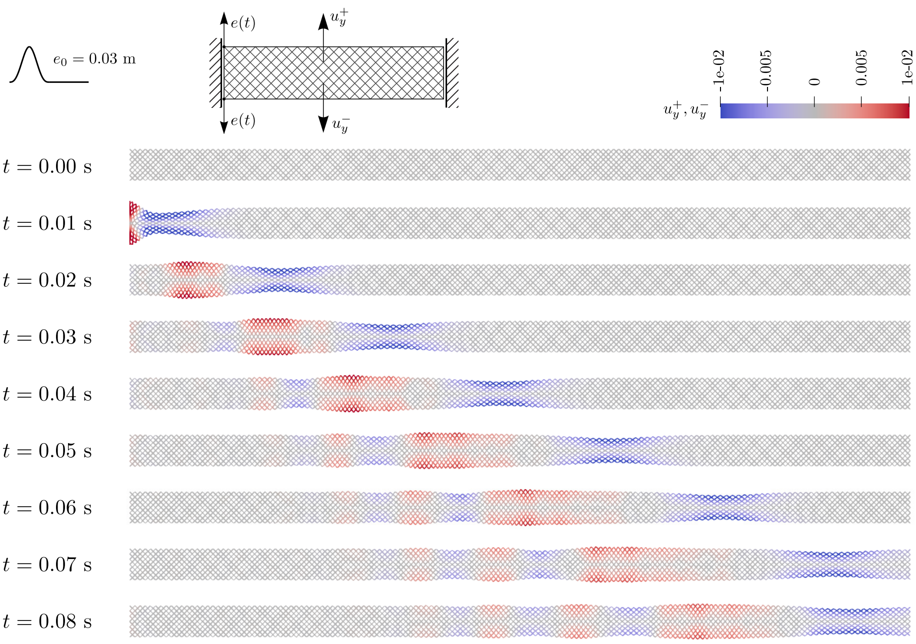

Figure 11: Point excitation with $n = 1, s_1 = 0.01\,\mathrm{s}$ and $e_0 = 0.03\,\mathrm{m}$.

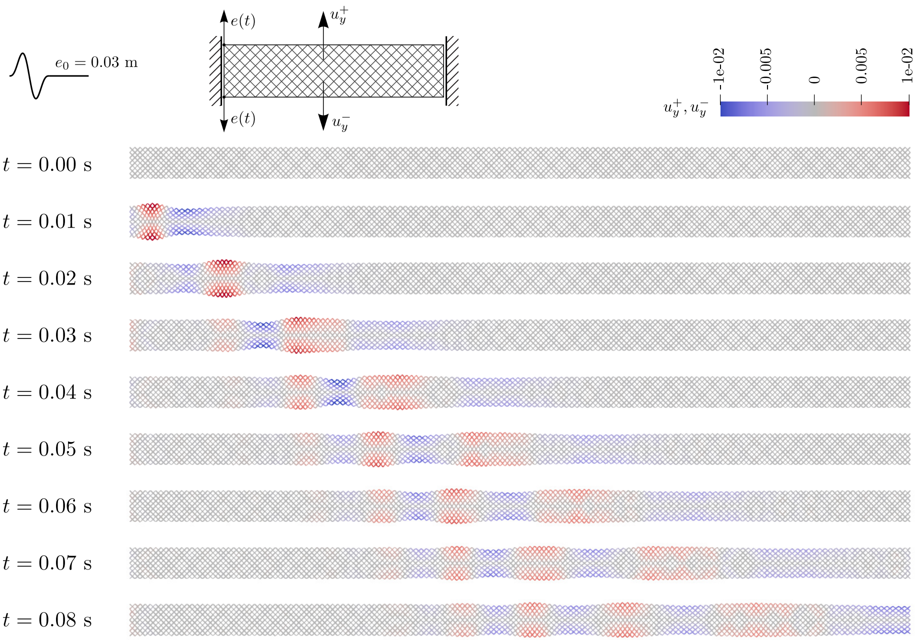

Figure 12: Point excitation with $n = 2, s_1 = 0.01\,\mathrm{s}$ and $e_0 = 0.03\,\mathrm{m}$.

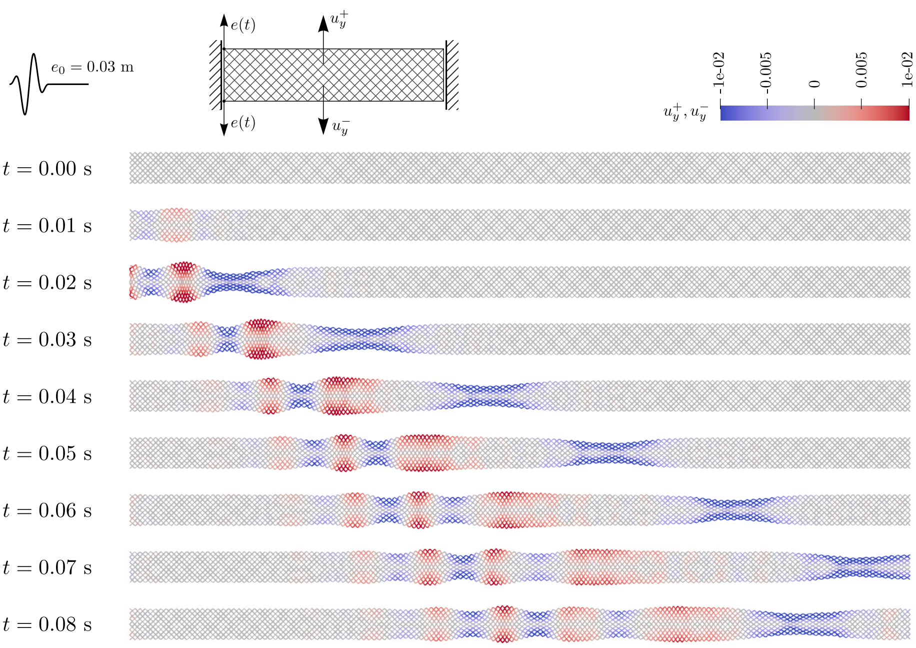

Figure 13: Point excitation with $n = 4, s_1 = 0.01\,\mathrm{s}$ and $e_0 = 0.03\,\mathrm{m}$.

matics and Mechanics of Solids, 8(1):51–73, 2003.

[2] U. Andreaus, M. Spagnuolo, T. Lekszycki, and S. R. Eugster. A Ritz approach for the static analysis of planar pantographic structures modeled with nonlinear Euler–Bernoulli beams. *Continuum Mechanics and Thermodynamics*, 30(5):1103–1123, 2018.

[3] M. Arnold and O. Brüls. Convergence of the generalized-α scheme for constrained mechanical systems. *Multibody System Dynamics*, 18(2):185–202, 2007.

[4] E. Barchiesi, F. dell'Isola, F. Hild, and P. Seppecher. Two-dimensional continua capable of large elastic extension in two independent directions: Asymptotic homogenization, numerical simulations and experimental evidence. *Mechanics Research Communications*, 103:103466, 2020.

[5] E. Barchiesi, S. R. Eugster, F. dell'Isola, and F. Hild. Large in-plane elastic deformations of bi-pantographic fabrics: asymptotic homogenization and experimental validation. *Mathematics and Mechanics of Solids*, 25(3):739–767, 2020.

[6] E. Barchiesi, S. R. Eugster, L. Placidi, and F. dell'Isola. Pantographic beam: a complete second gradient 1D-continuum in plane. *Zeitschrift für angewandte Mathematik und Physik*, 70(5):135:1–24, 2019.

[7] E. Barchiesi, M. Laudato, and F. Di Cosmo. Wave dispersion in non-linear pantographic beams. *Mechanics Research Communications*, 94:128–132, 2018.

[8] E. Barchiesi and L. Placidi. A review on models for the 3D statics and 2D dynamics of pantographic fabrics. In M. A. Sumbatyan, editor, *Wave dynamics and composite mechanics for microstructured materials and metamaterials*, pages 239–258. Springer, 2017.

[9] E. Barchiesi, M. Spagnuolo, and L. Placidi. Mechanical metamaterials: a state of the art. *Mathematics and Mechanics of Solids*, 24(1):212–234, 2019.

[10] G. Capobianco, S. R. Eugster, and T. Winandy. Modeling planar pantographic sheets using a nonlinear Euler–Bernoulli beam element based on B-spline functions. *Proceedings in Applied Mathematics and Mechanics*, 18(1):e201800220, 2018.

[11] M. De Angelo, E. Barchiesi, I. Giorgio, and B. E. Abali. Numerical identification of constitutive parameters in reduced-order bi-dimensional models for pantographic structures: application to out-of-plane buckling. *Archive of Applied Mechanics*, 89(7):1333–1358, 2019.

[12] F. dell'Isola, A. Della Corte, I. Giorgio, and D. Scerrato. Pantographic 2D sheets: Discussion of some numerical investigations and potential applications. *International Journal of Non-Linear Mechanics*, 80:200–208, 2016.

[13] F. dell'Isola, I. Giorgio, and U. Andreaus. Elastic pantographic 2D lattices: a numerical analysis on the static response and wave propagation. *Proceedings of the Estonian Academy of Sciences*, 64(3):219, 2015.

[14] F. dell'Isola, I. Giorgio, M. Pawlikowski, and N. L. Rizzi. Large deformations of planar extensible beams and pantographic lattices: heuristic homogenization, experimental and numerical examples of equilibrium. *Proceedings of the Royal Society of London A: Mathematical, Physical and Engineering Sciences*, 472(2185), 2016.

[15] F. dell'Isola, P. Seppecher, J. J. Alibert, and et al. Pantographic metamaterials: an example of mathematically driven design and of its technological challenges. *Continuum Mechanics and Thermodynamics*, 31(4):851–884, 2019.

[16] F. dell'Isola, P. Seppecher, and A. Madeo. How contact interactions may depend on the shape of Cauchy cuts in Nth gradient continua: approach "à la D'Alembert". *Zeitschrift für angewandte Mathematik und Physik*, 63(6):1119–1141, 2012.

[17] F. dell'Isola, P. Seppecher, M. Spagnuolo, and et al. Advances in pantographic structures: design, manufacturing, models, experiments and image analyses. *Continuum Mechanics and Thermodynamics*, 31(4):1231–1282, 2019.

[18] F. dell'Isola, M. Spagnuolo, E. Barchiesi, I. Giorgio, and P. Seppecher. Pantographic metamaterial: a (not so) particular case. In D. J. Steigmann and F. dell'Isola, editors, *Discrete and Continuum Models for Complex Metamaterials*, pages 103–138. Cambridge University Press, 2020.

[19] S. R. Eugster and J. Harsch. A variational formulation of classical nonlinear beam theories. In B. E. Abali and I. Giorgio, editors, *Develop-*

ments and Novel Approaches in Nonlinear Solid Body Mechanics, pages 95–121. Springer International Publishing, 2020.

[20] P. Germain. La méthodes des puissances virtuelles en mécanique des milieux continus - 1ère Partie, Théorie du second gradient. *Journal de Mécanique*, 12:235–274, 1973.

[21] P. Germain. The method of virtual power in the mechanics of continuous media, I: Second-gradient theory. *Mathematics and Mechanics of Complex Systems*, 8(2):153–190, 2020. Translated by M. Epstein and R. E. Smelser.

[22] I. Giorgio. Numerical identification procedure between a micro-Cauchy model and a macro-second gradient model for planar pantographic structures. *Zeitschrift für angewandte Mathematik und Physik*, 67(4):95:1–17, 2016.

[23] I. Giorgio. Lattice shells composed of two families of curved Kirchhoff rods: an archetypal example, topology optimization of a cycloidal metamaterial. *Continuum Mechanics and Thermodynamics*, pages 1–20, 2020.

[24] I. Giorgio, A. Della Corte, and F. dell'Isola. Dynamics of 1D nonlinear pantographic continua. *Nonlinear Dynamics*, 88(1):21–31, 2017.

[25] I. Giorgio, P. Harrison, F. dell'Isola, J. Alsayednoor, and E. Turco. Wrinkling in engineering fabrics: a comparison between two different comprehensive modelling approaches. *Proceedings of the Royal Society A: Mathematical, Physical and Engineering Sciences*, 474(2216):20180063, 2018.

[26] I. Giorgio, N. L. Rizzi, U. Andreaus, and D. J. Steigmann. A two-dimensional continuum model of pantographic sheets moving in a 3D space and accounting for the offset and relative rotations of the fibers. *Mathematics and Mechanics of Complex Systems*, 7(4):311–325, 2019.

[27] I. Giorgio, N. L. Rizzi, and E. Turco. Continuum modelling of pantographic sheets for out-of-plane bifurcation and vibrational analysis. *Proceedings of the Royal Society of London A: Mathematical, Physical and Engineering Sciences*, 473(2207):20170636:1–21, 2017.

[28] I. Giorgio, V. Varano, F. dell'Isola, and N. L. Rizzi. Two layers pantographs: A 2D continuum model accounting for the beams' offset and

relative rotations as averages in SO(3) Lie groups. *International Journal of Solids and Structures*, 216:43–58, 2021.

[29] J. Harsch and S. R. Eugster. Finite element analysis of planar nonlinear classical beam theories. In B. E. Abali and I. Giorgio, editors, *Developments and Novel Approaches in Nonlinear Solid Body Mechanics*, pages 123–157. Springer International Publishing, 2020.

[30] M. Laudato and E. Barchiesi. Non-linear dynamics of pantographic fabrics: modelling and numerical study. In M. A. Sumbatyan, editor, *Wave Dynamics, Mechanics and Physics of Microstructured Metamaterials: Theoretical and Experimental Methods*, pages 241–254. Springer International Publishing, 2019.

[31] M. Laudato, L. Manzari, I. Giorgio, M. Spagnuolo, and P. Göransson. Dynamics of pantographic sheet around the clamping region: experimental and numerical analysis. *Mathematics and Mechanics of Solids*, pages 1–23, 2021.

[32] F. Maurin, L. Dedè, and A. Spadoni. Isogeometric rotation-free analysis of planar extensible-elastica for static and dynamic applications. *Nonlinear Dynamics*, 81(1):77–96, 2015.

[33] F. Maurin, F. Greco, and W. Desmet. Isogeometric analysis for nonlinear planar pantographic lattice: discrete and continuum models. *Continuum Mechanics and Thermodynamics*, 31(4):1051–1064, 2019.

[34] R. D. Mindlin and N. N. Eshel. On first strain-gradient theories in linear elasticity. *International Journal of Solids and Structures*, 4(1):109–124, 1968.

[35] L. Piegl and W. Tiller. *The NURBS Book.* Springer-Verlag, second edition, 1997.

[36] L. Placidi, E. Barchiesi, E. Turco, and N. L. Rizzi. A review on 2D models for the description of pantographic fabrics. *Zeitschrift für angewandte Mathematik und Physik*, 67(5):121, 2016.

[37] P. Seppecher. Microscopic interpretation of strain-gradient and generalized continuum models. In A. Bertram and S. Forest, editors, *Mechanics of Strain Gradient Materials*, pages 71–99. Springer, 2020.

[38] R. A. Toupin. Elastic materials with couple-stresses. *Archive of Rational Mechanics and Analysis*, 11:385–414, 1962.

[39] C. Truesdell and R. Toupin. The classical field theories. In S. Flügge, editor, *Principles of Classical Mechanics and Field Theory*, volume III/1 of *Encyclopedia of Physics*. Springer, 1960.

[40] E. Turco. Stepwise analysis of pantographic beams subjected to impulsive loads. *Mathematics and Mechanics of Solids*, 26(1):62–79, 2021.

[41] E. Turco, F. dell'Isola, A. Cazzani, and N. L. Rizzi. Hencky-type discrete model for pantographic structures: numerical comparison with second gradient continuum models. *Zeitschrift für angewandte Mathematik und Physik*, 67(4):85, 2016.

[42] E. Turco, M. Golaszewski, I. Giorgio, and L. Placidi. Can a Hencky-type model predict the mechanical behaviour of pantographic lattices? In F. dell'Isola, M. Sofonea, and D. Steigmann, editors, *Mathematical Modelling in Solid Mechanics*, volume 69 of *Advanced Structured Materials*, pages 285–311. Springer, 2017.